

Multifunctional, Tunable Metal–Organic Framework Materials Platform for Bioimaging Applications

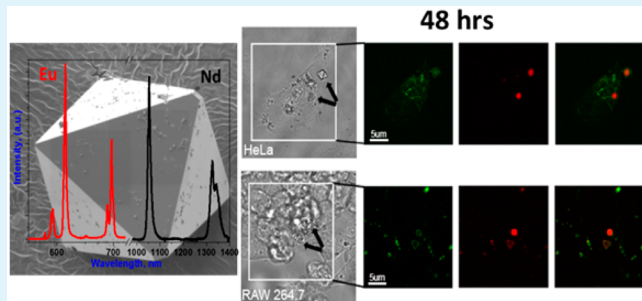
Dorina F. Sava Gallis,^{*†} Lauren E. S. Rohwer,[§] Mark A. Rodriguez,[‡] Meghan C. Barnhart-Dailey,[†] Kimberly S. Butler,[#] Ting S. Luk,^{||} Jerilyn A. Timlin,[†] and Karena W. Chapman[†]

[†]Nanoscale Sciences Department, [§]Microsystems Integration Department, [‡]Materials Characterization and Performance Department, ^{||}Nanostructure Physics Department, [†]Bioenergy and Defense Technology Department, and [#]Nanobiology Department, Sandia National Laboratories, Albuquerque, New Mexico 87185, United States

[†]X-ray Science Division, Advanced Photon Source, X-ray Science Division, Argonne National Laboratory, Argonne, Illinois 60439, United States

S Supporting Information

ABSTRACT: Herein, we describe a novel multifunctional metal–organic framework (MOF) materials platform that displays both porosity and tunable emission properties as a function of the metal identity (Eu, Nd, and tuned compositions of Nd/Yb). Their emission collectively spans the deep red to near-infrared (NIR) spectral region (~614–1350 nm), which is highly relevant for *in vivo* bioimaging. These new materials meet important prerequisites as relevant to biological processes: they are minimally toxic to living cells and retain structural integrity in water and phosphate-buffered saline. To assess their viability as optical bioimaging agents, we successfully synthesized the nanoscale Eu analog as a proof-of-concept system in this series. *In vitro* studies show that it is cell-permeable in individual RAW 264.7 mouse macrophage and HeLa human cervical cancer tissue culture cells. The efficient discrimination between the Eu emission and cell autofluorescence was achieved with hyperspectral confocal fluorescence microscopy, used here for the first time to characterize MOF materials. Importantly, this is the first report that documents the long-term conservation of the intrinsic emission in live cells of a fluorophore-based MOF to date (up to 48 h). This finding, in conjunction with the materials’ very low toxicity, validates the biocompatibility in these systems and qualifies them as promising for use in long-term tracking and biodistribution studies.



KEYWORDS: metal–organic framework, lanthanide, emission, bioimaging, near-infrared

1. INTRODUCTION

The quest to develop novel fluorescent probes for clinical diagnostics and to monitor biological processes *in vivo* has accelerated in recent years.¹ Deep-tissue imaging requires probes whose excitation and emission wavelengths have low optical attenuation in and do not excite fluorescence from the tissue. It is generally accepted that deep-red to near-infrared (NIR) wavelengths (~650–1450 nm) satisfy these requirements.² There is significant interest in developing novel materials whose excitation and emission wavelengths fall within the so-called second NIR window (1000–1350 nm),³ where absorption by blood and water are minimal and damage-free deep tissue penetration is possible.⁴ The use of the second NIR window allows for enhanced resolution of the vasculature in both normal limbs and tumors,⁵ the imaging of lymphatic systems,⁶ and the brain imaging of both tumors⁶ and traumatic brain injury through the intact skull.⁷

Known NIR-emitting fluorophores include organic dyes,⁸ quantum dots,⁹ and single-wall carbon nanotubes.¹⁰ Some of the main limitations associated with these systems include broad and

weak emissions and short lifetimes, which preclude their use in *in vivo* long-term tracking experiments.

Alternatively, probes based on lanthanide fluorescence offer significant advantages over the state-of-the-art materials to improve both the spectral and time-resolved signal discrimination from background autofluorescence due to (i) sharp and stable emissions, (ii) large effective Stokes shifts, and (iii) long-lived luminescent lifetimes.^{11,12} Also, they are generally regarded as nontoxic and have been shown to render only mild histological changes when used in high concentrations.¹³ Importantly, the luminescence of the lanthanide ions can be dramatically enhanced when sensitized by an organic chromophore via the antenna effect.^{14,15}

In this context, hybrid organic–inorganic materials, such as metal–organic frameworks (MOFs),¹⁶ can offer unique solutions to overcome the limitations of existing NIR emitting

Received: April 26, 2017

Accepted: June 14, 2017

Published: June 14, 2017

materials via (i) rational material design strategies through predetermined metal and ligand selection; (ii) emission tunability; and (iii) permanent porosity, which enables their use as advanced theranostic agents for imaging and cargo delivery in tandem, or the sensing of reactive species.

The luminescent properties of MOFs have been thoroughly investigated, primarily for sensing and light-emitting devices.^{17–19} Some of us have previously reported on their potential use in devices that operate at elevated temperatures, such as white light-emitting diodes for solid-state lighting.^{20,21} However, only a very limited number of studies have demonstrated their relevance as optical bioimaging agents.²² In fact, luminescence in the NIR has rarely been observed in MOFs,^{23–28} as the emission of NIR ions (Nd^{3+} , Yb^{3+} , and Er^{3+}) can be easily quenched due to a reduced energy gap between the ground state and the emitting state.⁴

In this study, we judiciously targeted a novel materials platform based on a predetermined rare-earth hexanuclear metal cluster, $\text{RE} = \text{Eu}, \text{Nd}, \text{Yb}, \text{Y}$, and Tb , as well as tuned compositions of Nd/Yb ($\text{Nd}_{0.67}/\text{Yb}_{0.33}$ and $\text{Nd}_{0.46}/\text{Yb}_{0.54}$) coordinated by 2,5-dihydroxyterephthalic acid. It is important to note that one of the greatest challenges that precludes the rational synthesis of MOFs with built-in structural features is the lack of control over the coordination geometry of the metal ions. Recently, Eddaoudi et al. pioneered the development of polynuclear rare-earth-based molecular building blocks and thoroughly detailed the important prerequisites for the systematic access to these molecular building blocks *in situ*.^{29–32}

The structure–function correlation in the materials reported here was investigated via in-depth characterization, including single-crystal X-ray diffraction (XRD), powder X-ray synchrotron scattering and pair distribution function analyses, microscopy, thermal analyses, and photoluminescence measurements. Particular emphasis was placed on evaluating the relevance to biorelated applications by (a) monitoring the stability under simulated physiological conditions, (b) evaluating the cytotoxicity to living cells, and (c) assessing the use as imaging agents via live cell imaging.

2. EXPERIMENTAL SECTION

All reactant materials were purchased from commercially available sources. They were used without further purification.

2.1. Materials Synthesis. *Synthesis of EuDOBDC, 1.* The reaction mixture containing $\text{EuCl}_3 \cdot 6\text{H}_2\text{O}$ (0.0689 g, 0.087 mmol), 2,5-dihydroxyterephthalic acid (DOBDC, 0.0544 g, 0.087 mmol), 2-fluorobenzoic acid (2-FBA, 0.5760 g, 4.12 mmol), N,N' -dimethylformamide (DMF, 8 mL), H_2O (2 mL), and HNO_3 (0.6 mL, 3.5 M in DMF) was placed in a 20 mL scintillation vial and was heated to 115 °C for 60 h at a rate of 1.5 °C/min. It was then cooled to room temperature at a cooling rate of 1 °C/min.

Synthesis of NdDOBDC, 2. The reaction mixture containing $\text{Nd}(\text{NO}_3)_3 \cdot 6\text{H}_2\text{O}$ (0.0412 g, 0.0940 mmol), 2,5-dihydroxyterephthalic acid (DOBDC, 0.0272 g, 0.137 mmol), 2-fluorobenzoic acid (2-FBA, 0.2880 g, 2.06 mmol), N,N' -dimethylformamide (DMF, 4 mL), and H_2O (1 mL) was placed in a 20 mL scintillation vial and was heated to 115 °C for 60 h at a rate of 1.5 °C/min. It was then cooled to room temperature at a cooling rate of 1 °C/min.

Synthesis of YbDOBDC, 3. The reaction mixture containing $\text{Yb}(\text{NO}_3)_3 \cdot \text{SH}_2\text{O}$ (0.0780 g, 0.174 mmol), 2,5-dihydroxyterephthalic acid (DOBDC, 0.0544 g, 0.275 mmol), 2-fluorobenzoic acid (2-FBA, 0.1948 g, 1.39 mmol), N,N' -dimethylformamide (DMF, 8.8 mL), H_2O (2 mL), and HNO_3 (0.4 mL, 3.5 M in DMF) was placed in a 20 mL scintillation vial and was heated to 115 °C for 60 h at a rate of 1.5 °C/min. It was then cooled to room temperature at a cooling rate of 1 °C/min.

Synthesis of YDOBDC, 4. The reaction mixture containing $\text{Y}(\text{NO}_3)_3 \cdot 6\text{H}_2\text{O}$ (0.1080 g, 0.311 mmol), 2,5-dihydroxyterephthalic acid (DOBDC, 0.0816 g, 0.412 mmol), 2-fluorobenzoic acid (2-FBA, 0.8640 g, 6.17 mmol), N,N' -dimethylformamide (DMF, 8 mL), H_2O (2 mL), and HNO_3 (0.6 mL, 3.5 M in DMF) was placed in a 20 mL scintillation vial and was heated to 115 °C for 60 h at a rate of 1.5 °C/min. It was then cooled to room temperature at a cooling rate of 1 °C/min.

Synthesis of TbDOBDC, 5. The reaction mixture containing $\text{Tb}(\text{NO}_3)_3 \cdot \text{SH}_2\text{O}$ (0.1224 g, 0.281 mmol), 2,5-dihydroxyterephthalic acid (DOBDC, 0.0816 g, 0.412 mmol), 2-fluorobenzoic acid (2-FBA, 0.8640 g, 6.17 mmol), N,N' -dimethylformamide (DMF, 8 mL), H_2O (2 mL), and HNO_3 (0.6 mL, 3.5 M in DMF) was placed in a 20 mL scintillation vial and was heated to 115 °C for 60 h at a rate of 1.5 °C/min. It was then cooled to room temperature at a cooling rate of 1 °C/min.

Synthesis of Nd_{0.67}Yb_{0.33}DOBDC, 6. The reaction mixture containing $\text{Nd}(\text{NO}_3)_3 \cdot 6\text{H}_2\text{O}$ (0.0381 g, 0.087 mmol), $\text{Yb}(\text{NO}_3)_3 \cdot \text{SH}_2\text{O}$ (0.0391 g, 0.087 mmol), 2,5-dihydroxyterephthalic acid (DOBDC, 0.0544 g, 0.275 mmol), 2-fluorobenzoic acid (2-FBA, 0.1948 g, 1.39 mmol), N,N' -dimethylformamide (DMF, 8.8 mL), H_2O (2 mL), and HNO_3 (0.4 mL, 3.5 M in DMF) was placed in a 20 mL scintillation vial and was heated to 115 °C for 60 h at a rate of 1.5 °C/min. It was then cooled to room temperature at a cooling rate of 1 °C/min.

Synthesis of Nd_{0.46}Yb_{0.54}DOBDC, 7. The reaction mixture containing $\text{Nd}(\text{NO}_3)_3 \cdot 6\text{H}_2\text{O}$ (0.0191 g, 0.0435 mmol), $\text{Yb}(\text{NO}_3)_3 \cdot \text{SH}_2\text{O}$ (0.0588 g, 0.131 mmol), 2,5-dihydroxyterephthalic acid (DOBDC, 0.0544 g, 0.275 mmol), 2-fluorobenzoic acid (2-FBA, 0.1948 g, 1.39 mmol), N,N' -dimethylformamide (DMF, 8.8 mL), H_2O (2 mL), and HNO_3 (0.4 mL, 3.5 M) was placed in a 20 mL scintillation vial and was heated to 115 °C for 60 h at a rate of 1.5 °C/min. It was then cooled to room temperature at a cooling rate of 1 °C/min.

Synthesis of EuDOBDC-Nanoparticles (NP), 1-NP. The reaction mixture containing $\text{EuCl}_3 \cdot 6\text{H}_2\text{O}$ (0.03445 g, 0.094 mmol), 2,5-dihydroxyterephthalic acid (DOBDC, 0.02720 g, 0.1375 mmol), 2-fluorobenzoic acid (2-FBA, 0.2880 g, 2.055 mmol), and N,N' -dimethylformamide (DMF, 4 mL) was placed in a 10 mL microwave vial and was heated to 175 °C for 15 min. A CEM Discover SP microwave was used for this experiment.

2.2. X-ray Single-Crystal Data Collection and Determination. The X-ray intensities were measured using a Bruker-D8 Venture dual-source diffractometer ($\text{Cu K}\alpha$, $\lambda = 1.5406 \text{ \AA}$) and complementary metal–oxide–semiconductor detector. Indexing and frame integration was performed using the APEX-III software suite.^{12a} Absorption correction was performed using face-indexing (numerical method), also within the APEX-III software. The structures were solved using SHELXL-2014/7 and refined using SHELXTL XLMP version 2014/7.

2.3. Powder X-ray Diffraction. Measurements were performed on a Siemens Kristalloflex D500 diffractometer with $\text{CuK}\alpha$ radiation ($\lambda = 1.54178 \text{ \AA}$).

2.4. Variable Temperature Powder X-ray Diffraction. High-temperature XRD experiments were performed using a Scintag PAD X₁ diffractometer (Thermo Electron Inc.; Waltham, MA) using $\text{Cu K}\alpha$ radiation, $\lambda = 0.15418 \text{ nm}$, an incident-beam mirror optic, a Peltier-cooled Ge solid-state detector, and a Buehler hot stage with a Pt/Rh heating strip and surround heater. Temperature calibration was performed using the thermal expansion behavior of alumina. Samples were heated in a static air, and scan parameters were 5–60° 2θ with a 0.05° step and a 3 s count-time.

2.5. Thermogravimetric–Mass Spectrometry Analyses. Measurements were conducted on a SDTQ600 TA Instruments, equipped with a mass spectrometer gas analyzer MS-ThermoStarTM from Pfeiffer Vacuum. The samples were heated to 105 °C at a 5 °C/min heating rate under continuous nitrogen flow.

2.6. High-Energy Synchrotron Scattering and Pair Distribution Function Analysis. X-ray scattering data suitable for diffraction and pair distribution function (PDF) analysis were collected at beamlines 11-ID-B at the Advanced Photon Source at Argonne National Laboratory. For PDF analysis, high-energy X-rays (11-ID-B, 58 keV, $\lambda = 0.2114 \text{ \AA}$) were used, in combination with a large amorphous silicon-

based area detector, to collect data to high values of momentum transfer ($Q_{\max} = 22 \text{ \AA}^{-1}$).^{33,34} The two-dimensional images were reduced to one-dimensional scattering data within fit2d. The PDFs, $G(r)$, were extracted within PDFgetX2, subtracting contributions from the background, Compton scattering, and fluorescence, to the total scattering data as described previously.³⁴ To separate the features in the PDF associated with the metal coordination, differential PDFs (dPDFs) were calculated, subtracting the PDF measured for the bulk ligand from that of the MOF. The position and area of features of interest within the dPDF were quantified by fitting Gaussian functions within fit2d.

For diffraction analysis, data were collected using a large amorphous silicon-based area detector placed a large distance (100 cm) from the sample to maximize angular resolution. The two-dimensional images were reduced to one-dimensional scattering data within fit2d.

2.7. Scanning Electron Microscopy–Energy-Dispersive Spectroscopy. Scanning electron microscopy (SEM) analyses were captured on a FEI NovaNano SEM 230 at various accelerating voltages between 1 and 20 kV. Energy-dispersive spectroscopy (EDS) analyses were collected on an EDAX Genesis Apex 2 with an Apollo SDD detector.

2.8. Transmission Electron Microscopy. Images from transmission electron microscopy (TEM) were taken on JEOL 1200EX transmission electron microscope with a maximum acceleration voltage of 120 kV. Prior to TEM measurements, samples were dispersed in absolute ethanol and deposited on a carbon-film-coated copper grid.

2.9. Sample-Activation and Gas-Adsorption Measurements. Prior to measuring the gas adsorption isotherms, the samples were immersed in 15 mL of methanol for 3 days, with the solvent being replenished every 24 h. Following this treatment, all samples were activated under a vacuum on a Micromeritics ASAP 2020 surface area and porosity analyzer, at 120 °C for 16 h. Nitrogen gas adsorption isotherms were measured at 77 K using nitrogen of ultrahigh purity (99.999%, obtained from Matheson Tri-Gas).

2.10. Photoluminescence Measurements. The photoluminescence (PL) emission and excitation spectra of powder samples of compound 1 were collected using a Horiba Jobin-Yvon Fluorolog-3 double-grating–double-grating fluorescence spectrophotometer in front-face mode. The powder samples of the visible light-emitting MOFs were placed in 4 in. long Pyrex NMR tubes for PLE and PL measurements.

Excitation spectra were collected by monitoring at the peak of the emission, and scanning over UV–visible wavelengths (320–550 nm). For the NIR PL measurements, powder samples of compounds 2, 6, and 7 were illuminated with an 808 nm diode laser using a long-pass dichroic beam splitter as a reflector. The PL transmitted through the splitter was directed to an Acton 2500 spectrophotometer (0.5 m focal length, 300 g/mm grating) equipped with liquid-nitrogen-cooled InGaAs linear array detector. Both the excitation source and the PL were focused through a common 0.65 NA objective. The NIR PL was collected from powder samples dispersed uniformly in a plastic Petri dish and placed under the objective.

2.11. Dynamic Light Scattering Measurements. Hydrodynamic size was acquired on a Malvern Zetasizer Nano-ZS equipped with a He–Ne laser (633 nm) and noninvasive backscatter optics (NIBS). All samples for dynamic light-scattering (DLS) measurements were suspended in various media (methanol, phosphate-buffered saline (PBS), and Dulbecco's modified Eagle medium (DMEM) + 10% fetal bovine serum (FBS)) at 0.5 mg/mL. Measurements were acquired at 25 °C and the refractive index was set to that of Eu (0.625). DLS measurements for each sample were obtained in triplicate. The Z-average diameter was used for all reported hydrodynamic size measurements.

2.12. Cytotoxicity Assessment. HeLa and RAW 264.7 cells (ATCC) were maintained in DMEM + 10% FBS. For cytotoxicity assessment, 5000 cells were plated per well in 100 μL in 96 well plates. Cells were allowed to adhere overnight. After the cells had adhered, fresh media containing MOF samples at varied concentration (0–500 μg/mL) were prepared. The MOF samples were suspended in dimethyl sulfoxide (DMSO); DMSO can adversely affect cell viability, so the addition of DMSO was held to 5 μL per 1 mL of sample. Cell exposure

was performed by the removal of media on the adherent cells and replacement with freshly prepared media containing MOF samples. Cells were exposed to MOF samples for 24 or 48 h at standard cell-culturing conditions (37 °C and 5% CO₂). After exposure, cytotoxicity was assessed using CellTiter-Glo 2.0 Assay (Promega) with luminescence measured by a BioTek microplate reader. The cell viability was calculated as a percentage of mock (DMSO-only) treated sample. Cytotoxicity measurements were performed in quadruplicate.

2.13. Hyperspectral Confocal Fluorescence Microscopy and Imaging of Pristine EuDOBDC-NP. Nanoparticles suspended in water were spread onto a glass slide and sealed with a coverslip. They were then imaged as described below.

2.14. Cell Incubation Experiments. RAW 264.7 mouse macrophage and HeLa human cervical cancer tissue culture cells were seeded for 24 h on glass poly-L-lysine coated coverslips at a density of 150 000 cells per well in a 6-well tissue-culture treated plate. After 24 h, a 10 mg/mL nanoparticle solution in DMSO for 24 h was added to the cells to a final concentration of 20 μg/mL in the well. Coverslips were mounted onto glass slides using silicon spacers containing a pool of DMEM + 10% FBS + 1% penicillin–streptomycin culture media and were immediately imaged. Samples were not kept under coverslips for more than 1 h per sample.

Spectral images of live cells were obtained on a custom hyperspectral confocal fluorescence microscope (HCFM).³⁵ Laser excitation (488 nm, Coherent, Inc.) was focused onto the cells using a 60× oil immersion objective (Nikon PlanApochromat, NA 1.4). Spectral data for each voxel of the image was dispersed using a prism spectrometer (500–800 nm) and collected with an electron-multiplied CCD camera (Andor Technologies, Inc.). During imaging, a combination of laser and stage scanning provided diffraction-limited voxels with spatial resolution of 240 nm × 240 nm × 600 nm and an integration time of 240 μs per spectrum.

HCFM images were preprocessed and underlying component spectra were extracted using multivariate curve resolution (MCR), as described elsewhere.^{36,37} HCFM images of both the HeLa and RAW cells containing 20 μg/mL nanoparticles were compiled into a composite image set. Principal component analysis of the preprocessed data set indicated three underlying spectral factors were present. A three-factor MCR model was developed that consisted of a flat baseline to describe detector offset and two fluorescence spectra: autofluorescence of the cells and the MOF nanoparticles. Concentration maps for each of the spectral components identified by MCR were predicted using classical least-squares analysis and represent the relative abundance and localization of each component within each image.

3. RESULTS AND DISCUSSION

3.1. Structural Characterization. In the first experiment, EuCl₃·6H₂O was reacted with DOBDC and 2-FBA in a DMF/H₂O system. This resulted in crystals with polyhedral morphology (Figure 1a). It should be noted that the addition of nitric acid was needed to improve the morphology of the crystalline phases reported herein, with the exception of Nd analog. Compound 1, EuDOBDC, was characterized and formulated by single crystal X-ray crystallography studies as Eu₆(μ₃-OH)₈(C₈H₄O₆)₅(C₈H₆O₆)₁(H₂O)₆·24 H₂O. The material is defined by a three-periodic framework with octahedral cages ~10.4 Å in diameter. The structure is based on the predesigned hydroxo-bridged cluster in which six metal atoms are coordinated by 12 DOBDC organic linkers, resulting in an overall 12-connected node. In the crystal structure of 1, the Eu metal ions adopt both eight- and nine-coordination geometries.

As compared to previous reports,^{29,30} the metal cluster accessed here exhibits a unique ligand binding mode. Specifically, 10 out of the 12 dicarboxylate bridging linkers bind in an anticipated bis-bidentate way, while the remaining 2 ligands coordinate to the metal ions in a monodentate fashion. This distinct behavior is likely correlated with the presence of the

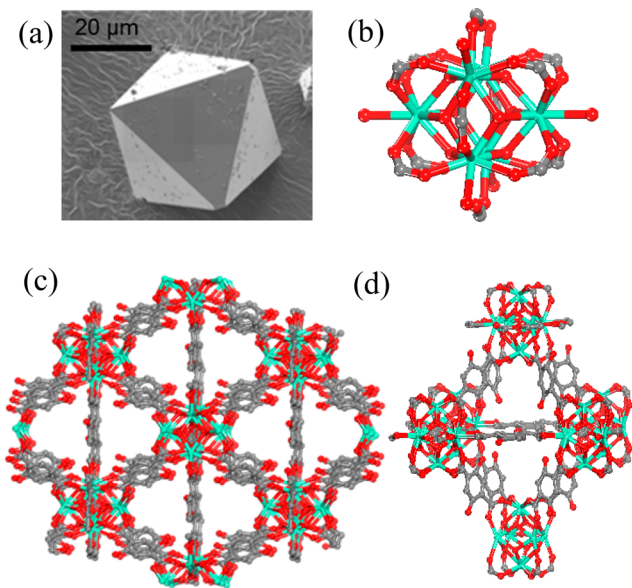


Figure 1. (a) SEM image of single-crystal of **1**; ball-and-stick depiction of (b) representative Eu hexanuclear cluster; (c) schematic view of the three-periodic framework; (d) octahedral cage.

hydroxyl groups in the close proximity of the carboxylates. The presence of the bridging disorder occurs in the *a–b* plane of the structure and serves as a true disorder of the DOBDC ligand, where the ligand bonds in a bidentate fashion on one cluster and bridges to the adjacent cluster to bond in a monodentate coordination. Each ligand residing in the *a–b* plane will bond in this manner with one side of the ligand as bidentate and the other side connecting as monodentate. This allows for two possible positions of the ligand between clusters, the same ligand lying side-by-side one another in the *a–b* plane, and only one of the two possible orientations is ever occupied at any given time. This slight alteration of the binding mode propagates a shift in the alignment of the clusters. As a result, there is a change in the symmetry from anticipated cubic crystal system to tetragonal. Hydrogen atoms and pore-solvent molecules have been omitted for clarity; atom color scheme is Eu, green; C, gray; and O, red.

The remaining coordination sites are occupied by a total of six water molecules per cluster. These water molecules can be removed by applying heat in a vacuum ($120\text{ }^{\circ}\text{C}$), generating coordinatively unsaturated metal centers. Importantly, only a very limited set of MOFs are known to exhibit this desirable property, which is highly useful for a variety of applications that are pertinent to tuning guest-framework interactions.³⁸ Furthermore, additional analogs were successfully synthesized, including the Nd, Yb, Y, and TbDOBDC versions as well as two mixed-metal systems, Nd_{0.67}/Yb_{0.33} and Nd_{0.46}/Yb_{0.54}DOBDC.

The isostructural nature in this materials platform was probed by a combination of synchrotron X-ray diffraction and pair distribution function analyses (Figure 2). There is a very good correlation between the calculated and experimental synchrotron powder X-ray diffraction studies on all compounds (Figure 2a). This finding illustrates both the phase purity and the structural similarities among the reported compounds.

Table 1 shows the unit cell lattice parameters for the analogs in this series, as refined from powder X-ray diffraction data. The X-ray single crystal data for the Eu structure was also included for comparison purposes. As expected, a gradual expansion of the

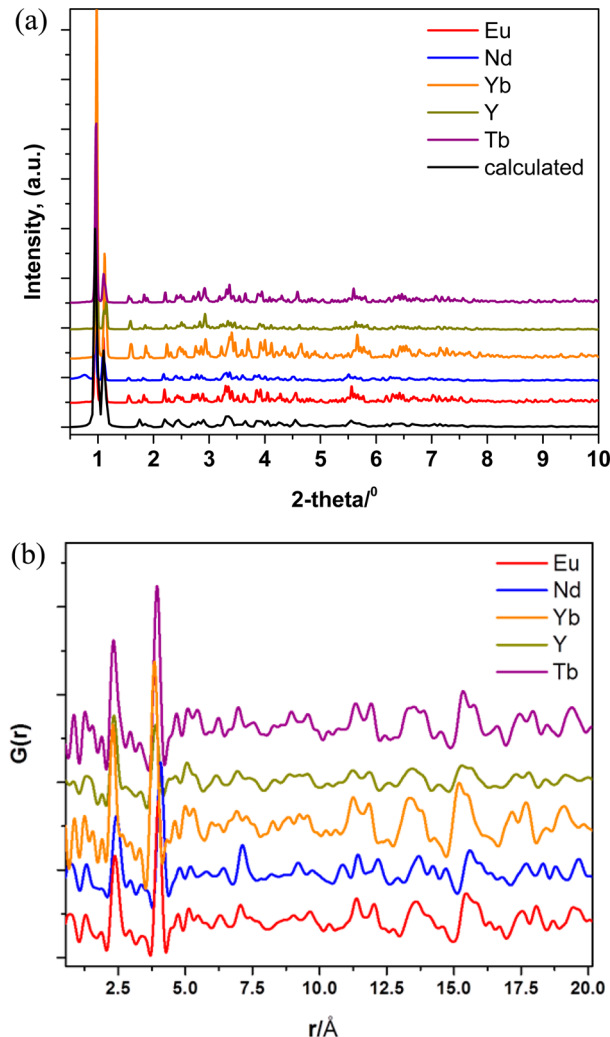


Figure 2. (a) Synchrotron X-ray diffraction data for compounds **1–5**, as compared with a calculated pattern of compound **1**, EuDOBDC (black); (b) PDF data on compounds **1–5**.

Table 1. Refined Unit Cell Lattice Parameters for Compounds **1–5**^a

compound	<i>a</i> (Å)	<i>c</i> (Å)	volume (Å ³)
EuDOBDC, 1	15.36 (1)	21.76 (2)	5133 (19)
EuDOBDC, 1 (single crystal)	15.56	21.33	5163
NdDOBDC, 2	15.50 (1)	21.89 (1)	5258 (7)
YbDOBDC, 3	15.07 (1)	21.29 (1)	4834 (7)
YDOBDC, 4	15.143 (7)	21.385 (7)	4904 (6)
TbDOBDC, 5	15.23 (2)	21.51 (1)	4993 (19)

^aError bars (1σ) are given in brackets.

unit cell volume is noted with the increase in the ionic radius for each of the RE elements used here: Nd > Eu > Tb > Y > Yb.

In addition, PDF analyses were conducted to better interrogate the local structure in these systems (Figure 2b). PDF is a powerful tool that provides detailed structural insights as a weighted histogram of atom–atom distances independent of sample crystallinity.³⁹ A pair of main peaks in the lower *r* region are distinguishable at ~ 2.5 and 4 \AA and are associated with the metal–O bond distance and the metal–metal bond, respectively. These findings demonstrate that the coordination profile in these

compounds is maintained at both long and short ranges, consistent with the expected isostructural nature.

Thermogravimetric analyses reveal that compounds **1–5** are stable until ~ 250 °C is reached (Figures S1–S5). A gradual weight loss beyond this point is associated with slow framework decomposition. Additionally, this process was probed in detail via temperature-controlled XRD for the EuDOBDC sample (Figure S6). The in situ XRD analysis reveals a clear breakdown of the diffraction pattern above 250 °C with a complete loss of the EuDOBDC reflections and the formation of what appears to be an amorphous phase. Not until ~ 600 °C does the appearance of a new crystalline phase of Eu₂O₃ appear.

The crystal structure of **1**, Figure 1c, reveals the potential for porous channels along the X and Y directions. The permanent porosity was investigated by measuring the nitrogen adsorption isotherms at 77 K on desolvated compounds **1–5** (Figure 3). All

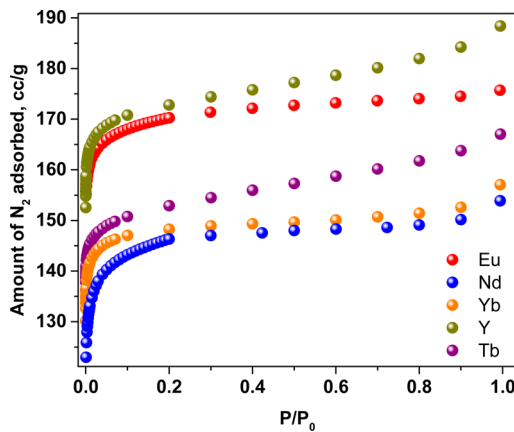


Figure 3. Nitrogen adsorption isotherms measured at 77 K on all samples.

five analogs adsorb N₂ and exhibit a type I isotherm, which is characteristic of microporous materials. The surface areas were evaluated using the Brunauer–Emmett–Teller (BET) and Langmuir methods and were found to vary between 587 m²/g for the Nd sample and 710 m²/g for the Y sample (Table 2).

Table 2. Surface-Area Analyses for Compounds **1–5**

compound	BET SA	Langmuir SA
EuDOBDC, 1	700 m ² /g	730 m ² /g
NdDOBDC, 2	587 m ² /g	620 m ² /g
YbDOBDC, 3	613 m ² /g	630 m ² /g
YDOBDC, 4	710 m ² /g	730 m ² /g
TbDOBDC, 5	630 m ² /g	650 m ² /g

To probe the relevance of using these materials as imaging agents, their chemical stability in water and PBS was evaluated. X-ray diffraction patterns show no change to the original structure after immersion in water for 7 days (Figure S7) and in PBS for 5 days (Figure S8). These are unique attributes in the context of MOFs, which generally lack robustness under these conditions.

3.2. Photoluminescence Properties. Trivalent lanthanides are known for their characteristic narrow-band emission. The photoluminescence excitation (PLE) and emission (PL) spectra of compound **1** in the as-synthesized and desolvated state are shown in panels a and b of Figure 4, respectively. Although the environment within the pores is different in each of these samples, they both exhibit red emission, characterized by

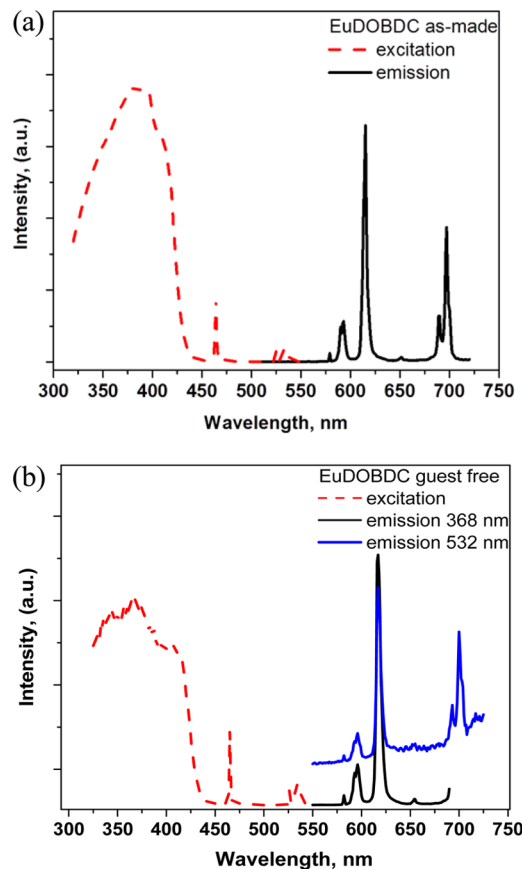


Figure 4. PLE and PL spectra for the (a) as-synthesized and (b) guest-free (desolvated) EuDOBDC sample, compound **1**; the spectra are offset for clarity. The emission was monitored at 614 nm for the PLE measurements.

narrowband peaks between 590–725 nm. These are assigned to the Eu³⁺ parity forbidden ⁵D – ⁷F transitions at ~ 590 nm (magnetic dipole transition ⁵D₀–⁷F₁) and electric dipole transitions at ~ 616 nm (⁵D₀–⁷F₂), 650 nm (⁵D₀–⁷F₃), and 700 nm (⁵D₀–⁷F₄).¹¹

The PL emission of compound **1** does not depend on the excitation wavelength. Figure 4b shows the PL spectra under 368 nm excitation, which sensitizes the Eu³⁺ via the excited states of the ligand; and 532 nm, which directly excites the 4f–4f transitions of Eu³⁺. Direct excitation has lower efficiency due to the very low molar extinction coefficient of Eu³⁺ at 532 nm. Next, the NIR-emitting compounds **2**, **6**, and **7** containing Nd³⁺ and Nd³⁺/Yb³⁺ were characterized.

Under 808 nm excitation, the Nd-based framework (Figure 5a; compound **2**) displays a sharp emission band at ~ 1060 nm, associated with ⁴F_{3/2}–⁴I_{11/2} transitions and a broader split band centered at 1325 nm, correlated with ⁴F_{3/2}–⁴I_{13/2} transitions. Nd³⁺ also has a very weak emission band at ~ 890 nm (not shown) and is attributed to the ⁴F_{3/2}–⁴I_{9/2} transitions.²⁸

To exploit the tunability uniquely intrinsic to MOFs, we designed mixed Nd/Yb samples at two distinct compositions: Nd_{0.67}Yb_{0.33}DOBDC, **6**, and Nd_{0.46}Yb_{0.54}DOBDC, **7**. As expected, compounds **6** and **7** display NIR emission from both the Nd and the Yb ions when excited at 808 nm. This wavelength directly excites the Nd ions, upon which energy is transferred nonradiatively from the ⁴F_{5/2} energy level of Nd³⁺ to the ⁵F_{5/2} energy level of Yb³⁺ to allow the narrow emission band at 980 nm, characteristic of Yb³⁺ (Figure 5b).

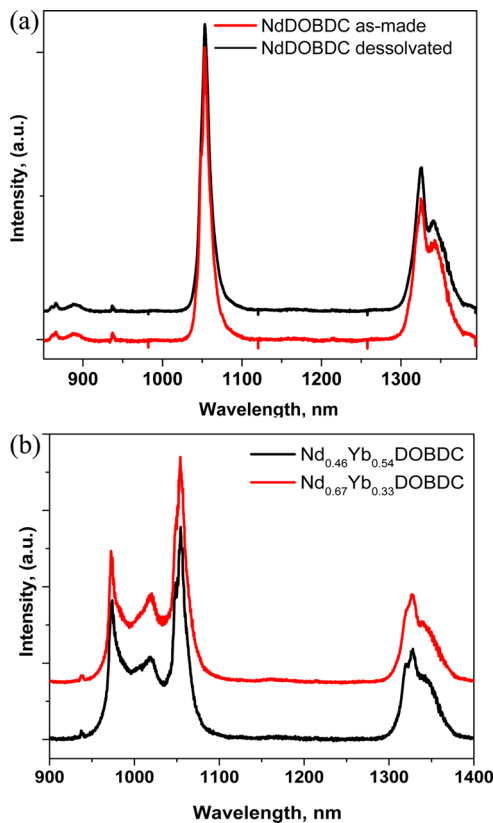


Figure 5. PL emission spectra at 808 nm excitation for (a) as-synthesized and guest-free (desolvated) NdDOBDC sample, compound 2; the spectra are offset for clarity. (b) Mixed-metal Nd_{0.67}Yb_{0.33}DOBDC, compound 6, and Nd_{0.46}Yb_{0.54}DOBDC samples, compound 7.

In an effort to probe the relevance of our newly designed materials platform to bioimaging applications, we first attempted the synthesis of the nanoscale analog for the red-emitting Eu-based framework. This choice was primarily dictated by the availability of conventional single photon microscopy techniques associated with emission in the visible range. The development of nano-MOFs for biomedicine is still scarcely reported, and only in recent years has some progress been made in this direction.⁴⁰ Here, we successfully synthesized the nanoscale analog of compound 1, EuDOBDC-NP, via a microwave-assisted approach.

TEM images reveal a fairly homogeneous distribution of particles in the 20–50 nm range (Figure 6a). Nitrogen adsorption studies were conducted on a desolvated sample and showed a BET surface area of 315 m²/g. A reduced amount of N₂ gas is adsorbed in EuDOBDC-NP as compared to the original EuDOBDC micron-sized particles. This phenomenon has been previously observed in other nanoparticle sized MOFs,⁴¹ and it may be associated with incomplete removal of pore guest molecules during the activation procedure.

To investigate the dispersion of EuDOBDC-NP in various environments, dynamic light-scattering measurements measurements were conducted on samples in methanol, PBS, and DMEM media + FBS (Table 3).

The particle size measured by DLS was larger than that based on the TEM measurement, likely due both to agglomeration of the EuDOBDC-NP in solution and to the nature of the DLS measurement itself. Unlike TEM, DLS measures the hydrodynamic diameter of the particles in solution, which includes the hydration layer and any associated proteins or stabilizers

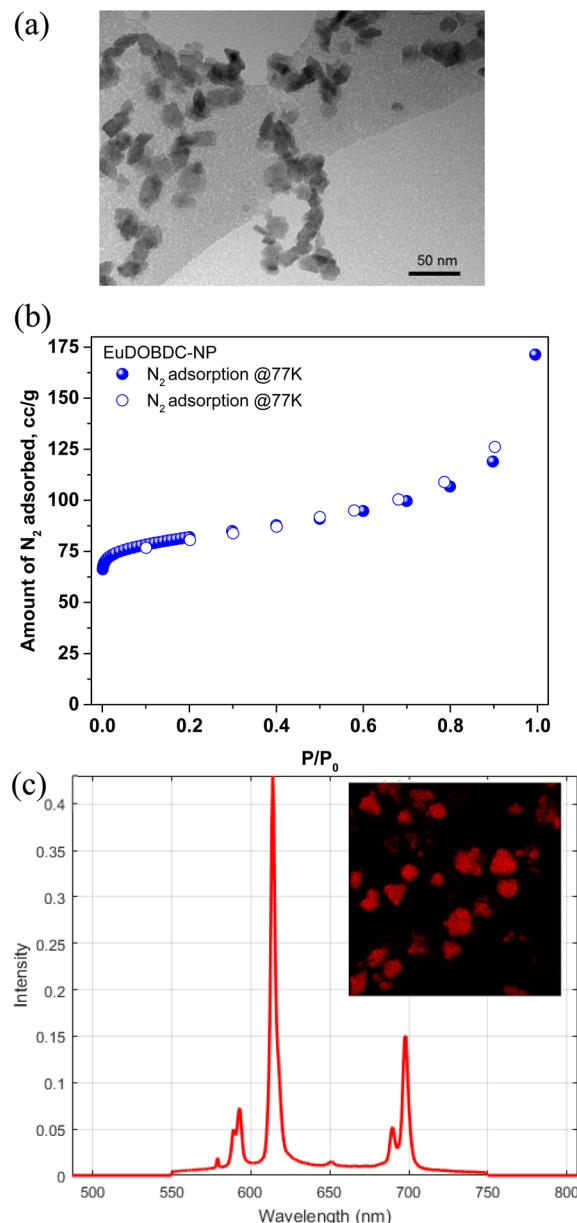


Figure 6. Structural characterization of EuDOBDC-NP: (a) TEM microscopy images; (b) N₂ sorption isotherm measured at 77 K; (c) emission spectrum and red-emitting EuDOBDC-NP as characterized by hyperspectral confocal fluorescence microscopy.

Table 3. Particle Size Distribution via DLS Measurements on the EuDOBDC-NP in Various Environments^a

solution	hydrodynamic Size (nm)	PdI
MeOH	446.3 (\pm 28.3)	0.213 (\pm 0.92)
PBS	963.7 (\pm 140.1)	0.446 (\pm 0.151)
DMEM media + FBS	1021 (\pm 254.0)	0.784 (\pm 0.36)

^aPdI: polydispersity index.

absorbed from the solution, leading to larger particle sizes than dried imaging measurements such as TEM.⁴² Additionally, the DLS measurement is based on light scattering, which is proportional to the sixth power of the particle diameter, and in the case of a polydisperse particle or agglomeration, it will result in the larger particles strongly influencing the final size measurement.⁴²

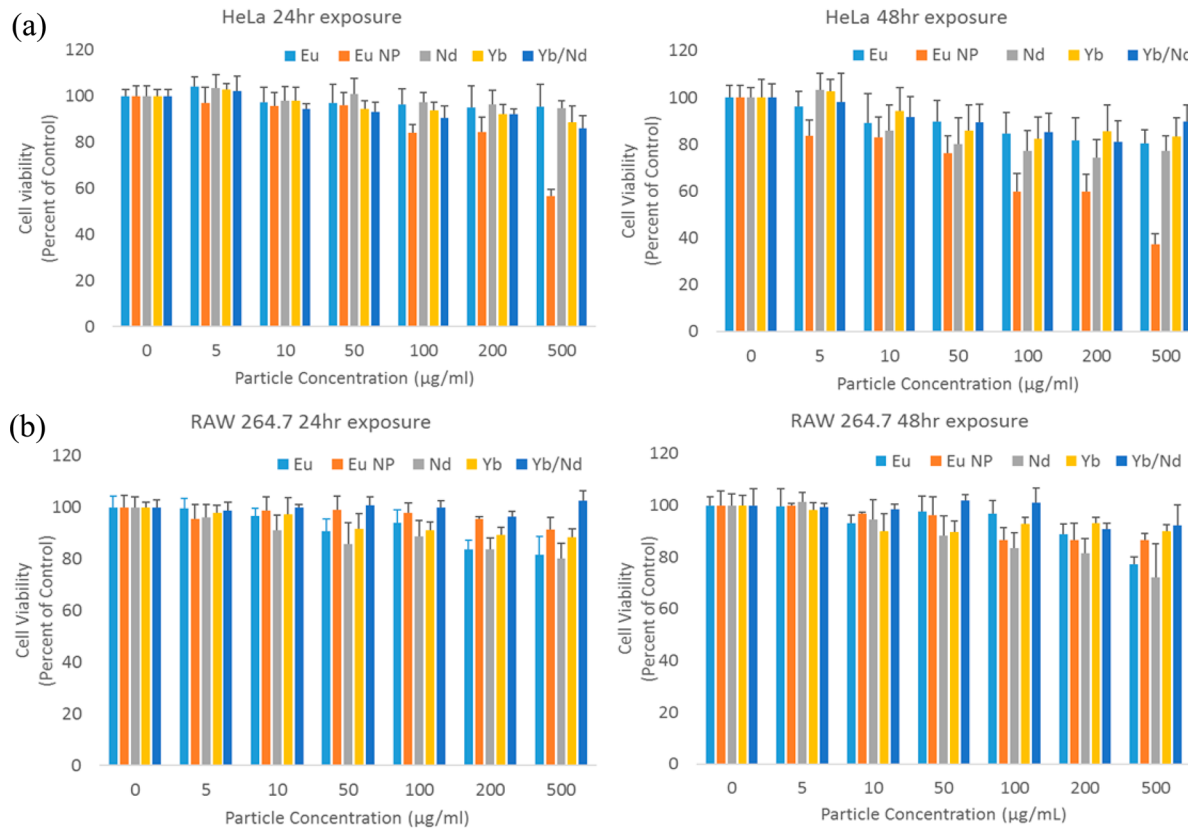


Figure 7. Cellular viability on (a) HeLa and (b) RAW 264.7 mouse macrophage cells after 24 h (left panel) and 48 h of incubation (right panel), showing minimal toxicity to both cell lines studied here. More than 80% of cells survive at both 24 and 48 h with doses up to 200 $\mu\text{g}/\text{mL}$.

A significant increase in size between DLS and TEM measurements of nanosized MOFs has also previously been reported.⁴³ Because most, if not all, therapeutic and imaging-based biological applications require dispersion in solution of some kind, measurement of the hydrodynamic size is important to understanding the behavior of the EuDOBDC-NP in biologically relevant environments. The particle-size increase is accentuated in biologically relevant solutions, such as PBS and DMEM media with FBS. This size increase correlates with amplified aggregation, most likely due to the particle's interaction with complex components in both PBS and cell culture media, previously observed with MOFs.⁴⁴ This suggests that additional surface modifications might be needed to improve the dispersion of the particles in biologically relevant solutions for biological applications.

Prior to conducting live cell imaging, we assessed the toxicity to mammalian cells in compounds **1**, **1-NP**, **2**, **3**, and **6** at both 24 and 48 h, at various concentrations up to 500 $\mu\text{g}/\text{mL}$ (Figure 7). The microsized particles (compounds **1**, **2**, **3**, and **6**) demonstrated little to no cytotoxicity regardless of composition, with greater than 80% of cells surviving at both 24 and 48 h with doses up to 200 $\mu\text{g}/\text{mL}$. The nanoscale Eu analog demonstrated increased toxicity compared to the microsized Eu particles. Enhanced toxicity on the nanoscale compared to the microscale has been documented for metal nanoparticles.⁴⁵ The particles displayed both a dose-dependent and a time-dependent toxicity, which was increased in human epithelial cells compared to the mouse macrophages. Differential toxicity between cell types has previously been observed with both other nanoparticles⁴⁶ and with other MOFs.⁴⁷ The mouse macrophages displayed greater than 80% cell viability at both 24 and 48 h, even with the 500 $\mu\text{g}/\text{mL}$

dose for 1-NP. Although an increase in toxicity was seen with the human epithelial cells, decreased cell viability below 80% was only seen with very high doses (500 $\mu\text{g}/\text{mL}$) or 48 h incubation times, demonstrating very low toxicity of the Eu nanoparticle overall. The toxicity demonstrated by the EuDOBDC-NP is equal to or significantly lower than the toxicity of many other nanoscale MOF formulations currently being developed for biological imaging or drug delivery.^{25,47,48}

Next, we undertook live cell imaging using a customized hyperspectral confocal fluorescence microscope. This technique is uniquely poised to characterize the interaction of nanoparticles with cells because it provides a direct measurement of the emission spectrum from each image voxel. MCR analysis was further used to extract the independently varying emission components. This is the first time this technique has been used to characterize MOF nanoparticles, although it has been previously implemented to assess interactions of quantum dots with cells.⁴⁹

Following an initial 2 h incubation period at a 20 $\mu\text{g}/\text{mL}$ concentration, nanoparticle uptake was observed only in a small portion of cells (~10%; Figure S13). Given that HCFM is a confocal microscope with axial resolution of approximately 600 nm and the approximate cell thickness is 5–10 μm , particles that were in focus and inside the cell membrane's periphery were considered to be internalized. The majority of cells displayed nanoparticles stuck to the cell surface and decorating the coverslip around the cells, as seen in the two top panels in Figure 8b.

Motivated by the interest to assess the relevance of these materials as long-term imaging agents, we further examined the particles following a 48 h incubation cycle at the 20 $\mu\text{g}/\text{mL}$ concentration. At this time point, 100% of HeLa cells and 74% of

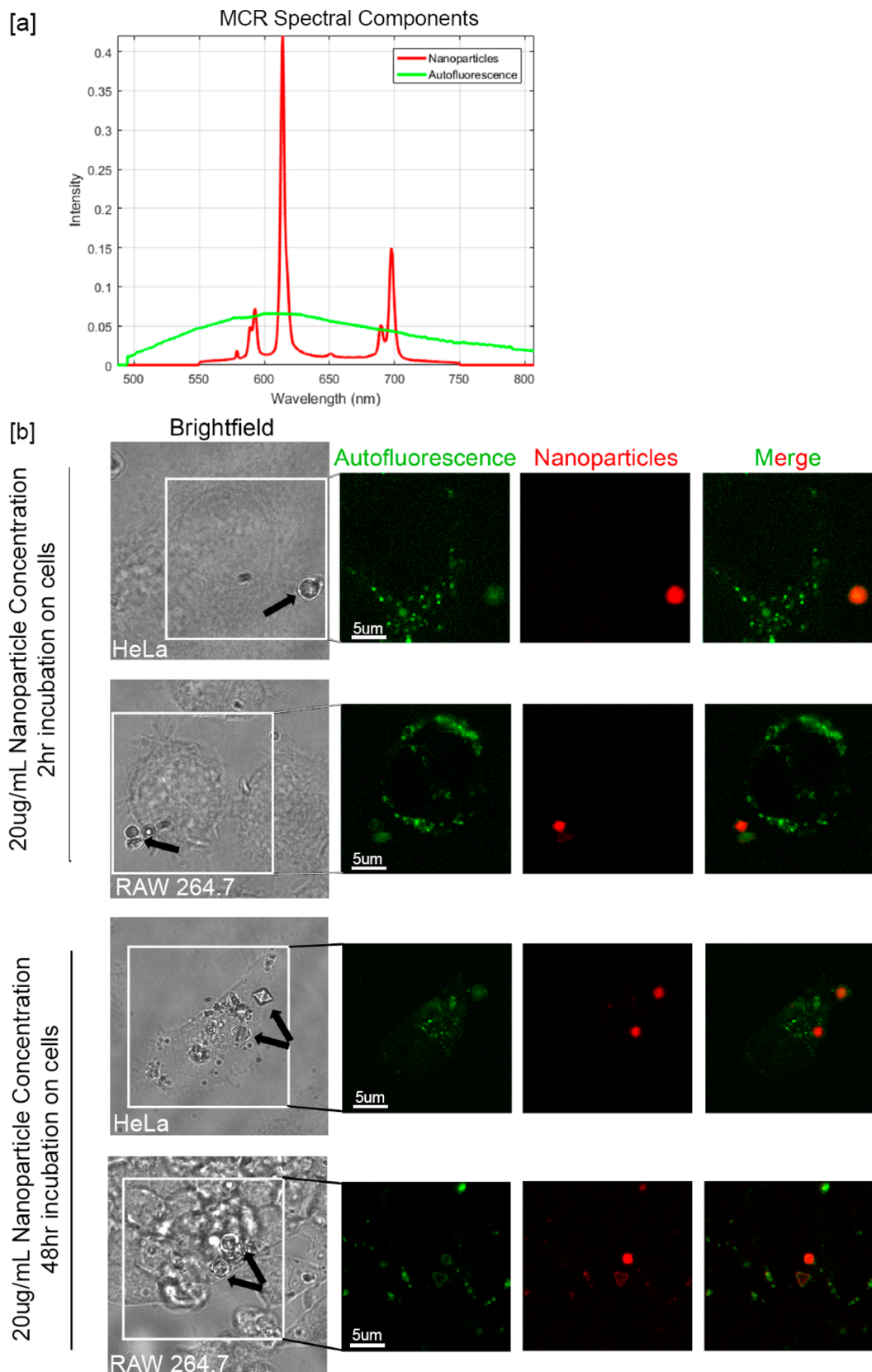


Figure 8. (a) MCR spectral components showing cell autofluorescence and the emission spectra of EuDOBC-NP. (b) Hyperspectral confocal fluorescence microscopy images of incubated EuDOBC-NP (at a concentration of 20 μ g/mL) with HeLa human cervical cancer cells and RAW 264.7 mouse macrophage cells for 2 h (top two panels) and 48 h (bottom two panels).

RAW cells had attached or incorporated nanoparticles, as seen in the bottom two panels in Figure 8b. At 48 h, some of the cells

appear to have taken up multiple particles, ranging from 2 to 11 particles per cell in HeLa and RAW cells. Importantly, the

spectrum of the nanoparticles was the same in solution and in tissue culture media and regardless of incubation time, indicating that the molecular composition remains unchanged in different environments. The intensity of the signal was markedly lower for the longer incubation time (48 h) indicating that perhaps some loss or degradation of the material under these conditions occurred. Correlating these findings with the cytotoxicity assays, this behavior can be associated with increased toxicity to the cell over time, possibly due to nanoparticle degradation in biological media. However, the red emission was still preserved in 25% of particles in HeLa cells and 39% in RAW 264.7 cells after 48 h in cell media.

This is an important finding, as this is the first example of a luminescent MOF that shows its emission preservation in live cells at this extended incubation time. Given the low cytotoxicity and the stable emission, the EuDOBDC-NP results indicate their suitability for long-term tracking experiments. However, the aggregation in biological media, shown in both the DLS and imaging studies, suggest that additional steps might be needed to further stabilize the particles.

5. CONCLUSIONS

In this study, we implemented a rational approach to the synthesis of made-to-order materials, showing that MOFs are uniquely suited materials systems for the addressing of current needs in the development of advanced fluorescent probes for *in vivo* bioimaging.

All analogs reported here are permanently porous and display tunable emission properties over a wide range, from deep red into the second NIR window. Importantly, the materials meet essential prerequisites as relevant to biorelated applications; they are minimally toxic to living cells and retain long-term crystallinity under relevant physiological conditions.

Initial proof-of-concept *in vitro* studies using RAW 264.7 mouse macrophage and HeLa human cervical cancer tissue culture cells demonstrate the viability of using these materials as bioimaging agents. Notably, the red emission is preserved, even at 48 h in both of the cell lines studied here, which, in combination with the low cytotoxicity, qualifies these probes as promising candidates for long-term biodistribution and tracking experiments.

Ongoing work is focused on the synthesis of the nanoparticle analogs for the NIR emitting compounds to evaluate their performance for *in vivo* small animal imaging. Additionally, we are exploiting their use as theranostic agents, as facilitated by the unique intrinsic luminescence–porosity combination in this tunable MOF materials platform.

■ ASSOCIATED CONTENT

Supporting Information

The Supporting Information is available free of charge on the ACS Publications website at DOI: [10.1021/acsami.7b05859](https://doi.org/10.1021/acsami.7b05859).

Thermogravimetric, differential scanning calorimetry, XRD, SEM–EDS, and hyperspectral confocal fluorescence microscopy analyses and crystal data. ([PDF](#))
CIF details. ([CIF](#))

■ AUTHOR INFORMATION

Corresponding Author

*E-mail: dfsava@sandia.gov.

ORCID

Dorina F. Sava Gallis: [0000-0001-6815-0302](https://orcid.org/0000-0001-6815-0302)

Notes

The authors declare no competing financial interest.

■ ACKNOWLEDGMENTS

The authors acknowledge Dr. Michael Sinclair for the use and maintenance of the hyperspectral confocal fluorescence microscope as well as Charles Pearce (TEM imaging and materials synthesis), James S. Chavez, and Grace Vincent (materials synthesis). This work is supported by the Laboratory Directed Research and Development Program at Sandia National Laboratories and was performed, in part, at the Center for Integrated Nanotechnologies, an Office of Science User Facility operated for the U.S. Department of Energy (DOE) Office of Science. Sandia National Laboratories is a multimission laboratory managed and operated by National Technology and Engineering Solutions of Sandia, LLC., a wholly owned subsidiary of Honeywell International, Inc., for the U.S. Department of Energy's National Nuclear Security Administration under contract no. DE-NA-0003525. Work done at Argonne and use of the Advanced Photon Source, an Office of Science User Facility operated for the U.S. DOE and Office of Science by Argonne National Laboratory, was supported by the U.S. DOE, contract no. DE-AC02-06CH11357.

■ REFERENCES

- (1) Pansare, V. J.; Hejazi, S.; Faenza, W. J.; Prud'homme, R. K. Review of Long-Wavelength Optical and Nir Imaging Materials: Contrast Agents, Fluorophores, and Multifunctional Nano Carriers. *Chem. Mater.* **2012**, *24*, 812–827.
- (2) Smith, A. M.; Mancini, M. C.; Nie, S. Bioimaging: Second Window for *In Vivo* Imaging. *Nat. Nanotechnol.* **2009**, *4*, 710–711.
- (3) Hemmer, E.; Benayas, A.; Legare, F.; Vetrone, F. Exploiting the Biological Windows: Current Perspectives on Fluorescent Bioprobe Emitting above 1000 Nm. *Nanoscale Horiz.* **2016**, *1*, 168–184.
- (4) Chen, Z.; Xu, H. Near-Infrared (Nir) Luminescence from Lanthanide(III) Complexes. In *Rare Earth Coordination Chemistry*; John Wiley & Sons, Ltd: Hoboken, NJ, 2010; pp 473–527.
- (5) Kim, D.; Lee, N.; Park, Y. I.; Hyeon, T. Recent Advances in Inorganic Nanoparticle-Based Nir Luminescence Imaging: Semiconductor Nanoparticles and Lanthanide Nanoparticles. *Bioconjugate Chem.* **2017**, *28*, 115–123.
- (6) Antaris, A. L.; Chen, H.; Cheng, K.; Sun, Y.; Hong, G.; Qu, C.; Diao, S.; Deng, Z.; Hu, X.; Zhang, B.; Zhang, X.; Yaghi, O. K.; Alamparambil, Z. R.; Hong, X.; Cheng, Z.; Dai, H. A Small-Molecule Dye for Nir-II Imaging. *Nat. Mater.* **2015**, *15*, 235–242.
- (7) Zhang, X.-D.; Wang, H.; Antaris, A. L.; Li, L.; Diao, S.; Ma, R.; Nguyen, A.; Hong, G.; Ma, Z.; Wang, J.; Zhu, S.; Castellano, J. M.; Wyss-Coray, T.; Liang, Y.; Luo, J.; Dai, H. Traumatic Brain Injury Imaging in the Second near-Infrared Window with a Molecular Fluorophore. *Adv. Mater.* **2016**, *28*, 6872–6879.
- (8) Escobedo, J. O.; Rusin, O.; Lim, S.; Strongin, R. M. Nir Dyes for Bioimaging Applications. *Curr. Opin. Chem. Biol.* **2010**, *14*, 64–70.
- (9) Pichaandi, J.; van Veggel, F. C. J. M. Near-Infrared Emitting Quantum Dots: Recent Progress on Their Synthesis and Characterization. *Coord. Chem. Rev.* **2014**, *263–264*, 138–150.
- (10) Welsher, K.; Liu, Z.; Sherlock, S. P.; Robinson, J. T.; Chen, Z.; Daranciang, D.; Dai, H. A Route to Brightly Fluorescent Carbon Nanotubes for near-Infrared Imaging in Mice. *Nat. Nanotechnol.* **2009**, *4*, 773–780.
- (11) Bunzli, J.-C. G.; Piguet, C. Taking Advantage of Luminescent Lanthanide Ions. *Chem. Soc. Rev.* **2005**, *34*, 1048–1077.
- (12) Moore, E. G.; Samuel, A. P. S.; Raymond, K. N. From Antenna to Assay: Lessons Learned in Lanthanide Luminescence. *Acc. Chem. Res.* **2009**, *42*, 542–552.

- (13) Nesmerak, K. Lanthanide/Actinide Toxicity In *Encyclopedia of Metalloproteins*, Uversky, V. N.; Kretsinger, R. H.; Permyakov, E. A., Eds.; Springer, Berlin, Germany, 2013; pp 1098–1103.
- (14) Ruiz-Medina, A.; Llorente-Martinez, E. J.; Ortega-Barrales, P.; Cerdova, M. L. F.-d. Lanthanide-Sensitized Luminescence as a Promising Tool in Clinical Analysis. *Appl. Spectrosc. Rev.* **2011**, *46*, 561–580.
- (15) Xu, L.-J.; Xu, G.-T.; Chen, Z.-N. Recent Advances in Lanthanide Luminescence with Metal-Organic Chromophores as Sensitizers. *Coord. Chem. Rev.* **2014**, *273–274*, 47–62.
- (16) Furukawa, H.; Cordova, K. E.; O’Keeffe, M.; Yaghi, O. M. The Chemistry and Applications of Metal-Organic Frameworks. *Science* **2013**, *341*, 1230444.
- (17) Allendorf, M. D.; Bauer, C. A.; Bhakta, R. K.; Houk, R. J. T. Luminescent Metal-Organic Frameworks. *Chem. Soc. Rev.* **2009**, *38*, 1330–1352.
- (18) Cui, Y.; Chen, B.; Qian, G. Lanthanide Metal-Organic Frameworks for Luminescent Sensing and Light-Emitting Applications. *Coord. Chem. Rev.* **2014**, *273–274*, 76–86.
- (19) Cui, Y.; Yue, Y.; Qian, G.; Chen, B. Luminescent Functional Metal-Organic Frameworks. *Chem. Rev.* **2012**, *112*, 1126–1162.
- (20) Sava, D. F.; Rohwer, L. E. S.; Rodriguez, M. A.; Nenoff, T. M. Intrinsic Broad-Band White-Light Emission by a Tuned, Corrugated Metal-Organic Framework. *J. Am. Chem. Soc.* **2012**, *134*, 3983–3986.
- (21) Sava Gallis, D. F.; Rohwer, L. E. S.; Rodriguez, M. A.; Nenoff, T. M. Efficient Photoluminescence Via Metal–Ligand Alteration in a New MOFs Family. *Chem. Mater.* **2014**, *26*, 2943–2951.
- (22) He, C.; Liu, D.; Lin, W. Nanomedicine Applications of Hybrid Nanomaterials Built from Metal–Ligand Coordination Bonds: Nanoscale Metal–Organic Frameworks and Nanoscale Coordination Polymers. *Chem. Rev.* **2015**, *115*, 11079–11108.
- (23) Guo, Z.; Xu, H.; Su, S.; Cai, J.; Dang, S.; Xiang, S.; Qian, G.; Zhang, H.; O’Keeffe, M.; Chen, B. A Robust near Infrared Luminescent Ytterbium Metal-Organic Framework for Sensing of Small Molecules. *Chem. Commun.* **2011**, *47*, 5551–5553.
- (24) White, K. A.; Chengelis, D. A.; Gogick, K. A.; Stehman, J.; Rosi, N. L.; Petoud, S. Near-Infrared Luminescent Lanthanide MOF Barcodes. *J. Am. Chem. Soc.* **2009**, *131*, 18069–18071.
- (25) Foucault-Collet, A.; Gogick, K. A.; White, K. A.; Villette, S.; Pallier, A.; Collet, G.; Kieda, C.; Li, T.; Geib, S. J.; Rosi, N. L.; Petoud, S. Lanthanide near Infrared Imaging in Living Cells with Yb³⁺ Nano Metal Organic Frameworks. *Proc. Natl. Acad. Sci. U. S. A.* **2013**, *110*, 17199–17204.
- (26) Zhao, D.; Zhang, J.; Yue, D.; Lian, X.; Cui, Y.; Yang, Y.; Qian, G. A Highly Sensitive near-Infrared Luminescent Metal-Organic Framework Thermometer in the Physiological Range. *Chem. Commun.* **2016**, *52*, 8259–8262.
- (27) White, K. A.; Chengelis, D. A.; Zeller, M.; Geib, S. J.; Szakos, J.; Petoud, S.; Rosi, N. L. Near-Infrared Emitting Ytterbium Metal-Organic Frameworks with Tunable Excitation Properties. *Chem. Commun.* **2009**, *4506–4508*.
- (28) Yang, J.; Yue, Q.; Li, G.-D.; Cao, J.-J.; Li, G.-H.; Chen, J.-S. Structures, Photoluminescence, up-Conversion, and Magnetism of 2d and 3d Rare-Earth Coordination Polymers with Multicarboxylate Linkages. *Inorg. Chem.* **2006**, *45*, 2857–2865.
- (29) Xue, D.-X.; Cairns, A. J.; Belmabkhout, Y.; Wojtas, L.; Liu, Y.; Alkordi, M. H.; Eddaoudi, M. Tunable Rare-Earth Fcu-MOFs: A Platform for Systematic Enhancement of CO₂ Adsorption Energetics and Uptake. *J. Am. Chem. Soc.* **2013**, *135*, 7660–7667.
- (30) Luebke, R.; Belmabkhout, Y.; Weselinski, L. J.; Cairns, A. J.; Alkordi, M.; Norton, G.; Wojtas, L.; Adil, K.; Eddaoudi, M. Versatile Rare Earth Hexanuclear Clusters for the Design and Synthesis of Highly-Connected Ftw-MOFs. *Chem. Sci.* **2015**, *6*, 4095–4102.
- (31) Guillerm, V.; Weseliński Łukasz, J.; Belmabkhout, Y.; Cairns, A. J.; D’Elia, V.; Wojtas, K.; Adil, K.; Eddaoudi, M. Discovery and Introduction of a (3,18)-Connected Net as an Ideal Blueprint for the Design of Metal–Organic Frameworks. *Nat. Chem.* **2014**, *6*, 673–680.
- (32) Alezi, D.; Peedikakkal, A. M. P.; Weseliński, L. J.; Guillerm, V.; Belmabkhout, Y.; Cairns, A. J.; Chen, Z.; Wojtas, L.; Eddaoudi, M. Quest for Highly Connected Metal–Organic Framework Platforms: Rare-Earth Polynuclear Clusters Versatility Meets Net Topology Needs. *J. Am. Chem. Soc.* **2015**, *137*, 5421–5430.
- (33) Chupas, P. J.; Qiu, X. Y.; Hanson, J. C.; Lee, P. L.; Grey, C. P.; Billinge, S. J. L. Rapid-Acquisition Pair Distribution Function (Ra-Pdf) Analysis. *J. Appl. Crystallogr.* **2003**, *36*, 1342–1347.
- (34) Chupas, P. J.; Chapman, K. W.; Lee, P. L. Applications of an Amorphous Silicon-Based Area Detector for High-Resolution, High-Sensitivity and Fast Time-Resolved Pair Distribution Function Measurements. *J. Appl. Crystallogr.* **2007**, *40*, 463–470.
- (35) Sinclair, M. B.; Haaland, D. M.; Timlin, J. A.; Jones, H. D. T. Hyperspectral Confocal Microscope. *Appl. Opt.* **2006**, *45*, 6283–6291.
- (36) Jones, H. D. T.; Haaland, D. M.; Sinclair, M. B.; Melgaard, D. K.; Collins, A. M.; Timlin, J. A. Preprocessing Strategies to Improve MrC Analyses of Hyperspectral Images. *Chemom. Intell. Lab. Syst.* **2012**, *117*, 149–158.
- (37) Haaland, D. M.; Jones, H. D. T.; Timlin, J. A., Chapter 12 - Experimental and Data Analytical Approaches to Automating Multivariate Curve Resolution in the Analysis of Hyperspectral Images. In *Data Handl. Sci. Technol.*, Cyril, R., Ed.; Elsevier: Philadelphia, PA, 2016; Vol. Vol. 30, pp 381–408.
- (38) Chen, B.; Xiang, S.; Qian, G. Metal–Organic Frameworks with Functional Pores for Recognition of Small Molecules. *Acc. Chem. Res.* **2010**, *43*, 1115–1124.
- (39) Chapman, K. W. Emerging Operando and X-Ray Pair Distribution Function Methods for Energy Materials Development. *MRS Bull.* **2016**, *41*, 231–240.
- (40) Giménez-Marqués, M.; Hidalgo, T.; Serre, C.; Horcajada, P. Nanostructured Metal–Organic Frameworks and Their Bio-Related Applications. *Coord. Chem. Rev.* **2016**, *307* (2), 342–360.
- (41) Cravillon, J.; Münzer, S.; Lohmeier, S.-J.; Feldhoff, A.; Huber, K.; Wiebcke, M. Rapid Room-Temperature Synthesis and Characterization of Nanocrystals of a Prototypical Zeolitic Imidazolate Framework. *Chem. Mater.* **2009**, *21*, 1410–1412.
- (42) Fissan, H.; Ristig, S.; Kaminski, H.; Asbach, C.; Epple, M. Comparison of Different Characterization Methods for Nanoparticle Dispersions before and after Aerosolization. *Anal. Methods* **2014**, *6*, 7324–7334.
- (43) Hirsche, P.; Prei; Auras, F.; Pick, A.; Volkner, J.; Valdeperez, D.; Witte, G.; Parak, W. J.; Radler, J. O.; Wuttke, S. Exploration of MOF Nanoparticle Sizes Using Various Physical Characterization Methods - Is What You Measure What You Get? *CrystEngComm* **2016**, *18*, 4359–4368.
- (44) Orellana-Tavra, C.; Marshall, R. J.; Baxter, E. F.; Lazaro, I. A.; Tao, A.; Cheetham, A. K.; Forgan, R. S.; Fairén-Jimenez, D. Drug Delivery and Controlled Release from Biocompatible Metal-Organic Frameworks Using Mechanical Amorphization. *J. Mater. Chem. B* **2016**, *4*, 7697–7707.
- (45) Semisch, A.; Hartwig, A. Copper Ions Interfere with the Reduction of the Water Soluble Tetrazolium Salt-8. *Chem. Res. Toxicol.* **2014**, *27*, 169–171.
- (46) Sohaebuddin, S. K.; Thevenot, P. T.; Baker, D.; Eaton, J. W.; Tang, L. Nanomaterial Cytotoxicity Is Composition, Size, and Cell Type Dependent. *Part. Fibre Toxicol.* **2010**, *7*, 22–22.
- (47) Tamames-Tabar, C.; Cunha, D.; Imbuluzqueta, E.; Ragon, F.; Serre, C.; Blanco-Prieto, M. J.; Horcajada, P. Cytotoxicity of Nanoscaled Metal-Organic Frameworks. *J. Mater. Chem. B* **2014**, *2*, 262–271.
- (48) Hu, Q.; Yu, J.; Liu, M.; Liu, A.; Dou, Z.; Yang, Y. A Low Cytotoxic Cationic Metal–Organic Framework Carrier for Controllable Drug Release. *J. Med. Chem.* **2014**, *57*, 5679–5685.
- (49) Aaron, J. S.; Greene, A. C.; Kotula, P. G.; Bachand, G. D.; Timlin, J. A. Advanced Optical Imaging Reveals the Dependence of Particle Geometry on Interactions between CdSe Quantum Dots and Immune Cells. *Small* **2011**, *7*, 334–341.